Sn 5s^2 lone pairs and the electronic structure of tin sulphides: A photoreflectance, high-energy photoemission, and theoretical investigation

Leanne A. H. Jones [1], Wojciech M. Linhart [2], Nicole Fleck [1], Jack E. N. Swallow,[1] Philip A. E. Murgatroyd [1],
Huw Shiel,[1] Thomas J. Featherstone,[1] Matthew J. Smiles [1], Pardeep K. Thakur [3], Tien-Lin Lee,[3] Laurence J. Hardwick [4],
Jonathan Alaria [1], Frank Jäckel [1], Robert Kudrawiec [2], Lee A. Burton,[5] Aron Walsh [6,7], Jonathan M. Skelton [8],
Tim D. Veal [1,*] and Vin R. Dhanak[1]

[1]*Stephenson Institute for Renewable Energy and Department of Physics, University of Liverpool, Liverpool L69 7ZF, United Kingdom*
[2]*Department of Semiconductor Materials Engineering, Faculty of Fundamental Problems of Technology, Wroclaw University of Science and Technology, Wybrzeze Wyspianskiego 27, 0-370 Wroclaw, Poland*
[3]*Diamond Light Source Ltd., Diamond House, Harwell Science and Innovation Campus, Didcot, Oxfordshire OX11 0DE, United Kingdom*
[4]*Stephenson Institute for Renewable Energy and Department of Chemistry, University of Liverpool, Liverpool L69 7ZF, United Kingdom*
[5]*International Centre for Quantum and Molecular Structures, Physics Department, Shanghai University, Shanghai, 200444 China*
[6]*Department of Materials, Imperial College London, London SW7 2AZ, United Kingdom*
[7]*Department of Materials Science and Engineering, Yonsei University, Seoul 03722, Korea*
[8]*Department of Chemistry, University of Manchester, Oxford Road, Manchester M13 9PL, United Kingdom*

The effects of Sn 5s lone pairs in the different phases of Sn sulphides are investigated with photoreflectance, hard x-ray photoemission spectroscopy (HAXPES), and density functional theory. Due to the photon energy-dependence of the photoionization cross sections, at high photon energy, the Sn 5s orbital photoemission has increased intensity relative to that from other orbitals. This enables the Sn 5s state contribution at the top of the valence band in the different Sn-sulphides, SnS, Sn$_2$S$_3$, and SnS$_2$, to be clearly identified. SnS and Sn$_2$S$_3$ contain Sn(II) cations and the corresponding Sn 5s lone pairs are at the valence band maximum (VBM), leading to ∼1.0–1.3 eV band gaps and relatively high VBM on an absolute energy scale. In contrast, SnS$_2$ only contains Sn(IV) cations, no filled lone pairs, and therefore has a ∼2.3 eV room-temperature band gap and much lower VBM compared with SnS and Sn$_2$S$_3$. The direct band gaps of these materials at 20 K are found using photoreflectance to be 1.36, 1.08, and 2.47 eV for SnS, Sn$_2$S$_3$, and SnS$_2$, respectively, which further highlights the effect of having the lone-pair states at the VBM. As well as elucidating the role of the Sn 5s lone pairs in determining the band gaps and band alignments of the family of Sn-sulphide compounds, this also highlights how HAXPES is an ideal method for probing the lone-pair contribution to the density of states of the emerging class of materials with ns^2 configuration.

I. INTRODUCTION

Group 13 through group 16 post-transition metals and metalloids within compounds exhibit two oxidation states; the group oxidation state, *N*, and a lower *N*-2 oxidation state; the latter being due to chemically inert, but frequently stereochemically active, lone-pair electrons. The occupation of these ns^2 lone pairs means that the materials have vastly different properties from when the cation has the group oxidation state. Compounds that have the lone-pair configuration are used in many different applications, for example,

optoelectronic materials, such as bismuth and antimony-based oxyhalides and chalcogenides [1]; photocatalysts, Bi$_2$O$_3$ combined with V$_2$O$_5$, where lone pairs are important for the photoactivity of the material [2,3]; chemical energy storage, β-PbO$_2$ [4]; and solar absorbers, lead (II) halides and chalcogenides, germanium chalcogenides, bismuth sulphide and copper-antimony- and copper-bismuth-chalcogenides [5–8]. Therefore, a good understanding of these materials is essential.

What these materials have in common is a distorted crystal structure accompanied by the ns^2 configuration. The distortion means that the structures are noncentrosymmetric, which results in symmetry-allowed mixing of the s and p states that stabilizes the distortion [9]. The lone pair is usually projected into a void within the structure and energetically is located at the valence band maximum (VBM) of these materials.

The presence of lone pairs changes the properties of a material. A good representation of these changes is given by the tin sulphide phases. As with several other group 13–16
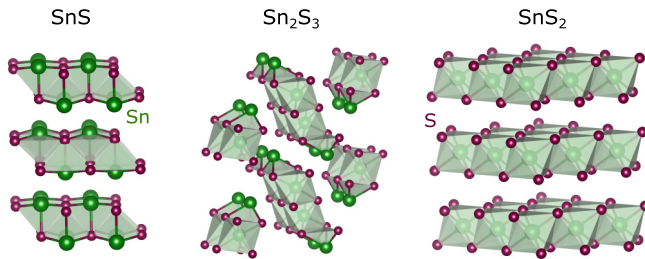

FIG. 1. Ground-state structures of the tin sulphides used for this study. SnS (left), Sn_2S_3 (middle), and SnS_2 (right). The tin atoms are green and the sulfur atoms are purple.
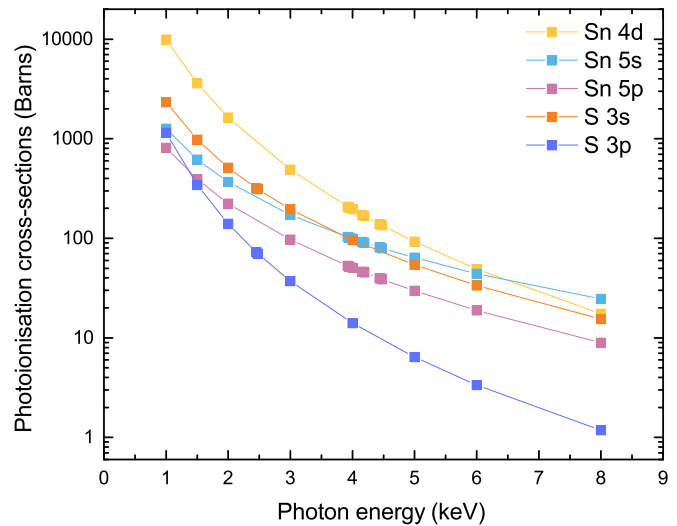

FIG. 2. Photoionization cross sections for Sn $4d$, $5s$, and $5p$, demonstrating the advantage of using higher photon energies to probe the ns^2 lone-pair configuration in Sn sulphides.

metals and metalloids [9], Sn can be found in two oxidation states, N and N-2, where N is in the group valence: For the case of tin, these are Sn(II) and Sn(IV) with electron configurations of $[Kr]4d^{10}5s^25p^0$ and $[Kr]4d^{10}5s^05p^0$, respectively. This means that several different phases of the Sn sulphides can be realized. The ones used for this paper are shown in Fig. 1: (1) orthorhombic SnS with the *Pnma* space group, (2) Sn_2S_3 that also has the *Pnma* space group, and (3) 2H-SnS_2 which has the $P\bar{3}m1$ space group.

SnS has an orthorhombic herzenbergite structure where Sn^{2+} coordinates to three S^{2-} ions and a lone pair occupies the last tetrahedral position. Tin sulphide (SnS) exhibits all the requirements for a photovoltaic absorber, such as its elements are abundant and nontoxic, it has a high optical absorption coefficient and its absorption onset coincides with the Shockley-Queisser limit within the AM 1.5 solar spectrum with its direct band gap of $\sim$1.3 eV [10–13]. The record power conversion efficiency for SnS solar cells is 4.8% [14]. One of the limitations to the performance of SnS is the secondary phases (Sn_2S_3 and SnS_2) that can form during growth. The reduction of Sn(IV) to Sn(II) in copper zinc tin sulphide (CZTS) has also been shown to produce defects that are deleterious to the photovoltaic performance of CZTS [15].

SnS_2 on the other hand, consists of a hexagonal arrangement of six S^{2-} ions coordinated to each Sn^{4+} ion. The sulfur atoms are in an octahedral formation around the Sn atom. Despite being detrimental to the photovoltaic performance for SnS, SnS_2 has its own uses for visible light water splitting [16] because of its two-dimensional nature and band gap of $\sim$2.3 eV [17–19].

Both Sn oxidation states can be found in one compound. An example of this is Sn_2S_3. Its structure is comprised of Sn_2S_3 chains where the Sn atoms in the center of the chains are octahedrally coordinated and thus in the Sn(IV) oxidation state whereas the Sn atoms at the chain ends are found in the Sn(II) oxidation state as they have adopted a trigonal pyramidal arrangement. Therefore, Sn_2S_3 also has lone pairs similar to SnS. This material with multivalent Sn has not been studied as extensively as the other two Sn sulphides.

It has been shown previously that hard x-ray photoemission spectroscopy (HAXPES) can be a favorable technique for probing the s lone pair states in β-PbO_2 [4]. From the calculations of Scofield [20] and Yeh and Lindau [21], it is known that the photoionization cross sections of s orbitals generally fall less rapidly than those of p, d, or f orbitals with increasing photon energy. For example, the cross section of

Sn $4d$ is 3644 Barns at 1486.7 eV and 49 Barns at 6000 eV, whereas for Sn $5s$ the cross section is 628 Barns at 1486.7 eV and 44 Barns at 6000 eV. This illustrates the different rates of decay of the photoionization cross section with photon energy for different orbitals. The variation of the cross sections of the Sn and S orbitals is shown in Fig. 2.

The photoionization probabilities decrease with increasing incident photon energy due to the decrease in the wavelength of the continuum states as the electron kinetic energy increases. This wavelength becomes increasingly comparable with the radial extension of the valence orbitals, resulting in cancellation of terms contributing to the transition moment. In general, s cross sections decrease less rapidly because the orbitals are more contracted [22]. Therefore, exploiting this by using synchrotron-generated hard x rays allows s-state lone pairs in such materials to be probed more effectively than with soft (1486.7 eV) x rays.

Previous work has reported the use of 1486.7 eV photoemission to identify the tin sulphide phases [23]. At the valence band edge, a small intensity is seen for the lone pair containing Sn sulphides. However, it is seen that the valence band is dominated by S $3p$ orbitals due to the relative cross sections. Figure 2 shows the photoionization cross sections of the Sn $4d$, $5s$, $5p$, S $3s$, and $3p$ orbitals depicting how the cross section of the S $3p$ states falls much more rapidly than that of Sn $5s$ with increasing photon energy.

Therefore, this paper presents a report of HAXPES measurements of the electronic structure of Sn sulphides. It highlights the usefulness of HAXPES when determining the electronic structure of lone-pair configurations as the relative strength of the corresponding s state will be greater than when laboratory-based x rays are utilized; not just for Sn sulphides, but for all ns^2 systems. It also presents photoreflectance (PR) measurement of Sn_2S_3 as well as PR measurements for both SnS and SnS_2 where the fundamental direct band gaps are revealed. These measurements emphasize the effects of the presence of lone pairs on the band gap.

II. METHODS

Single crystals of the three tins sulphides were grown by chemical vapor transport, further details of which can be found elsewhere for SnS and Sn_2S_3 [24] and for SnS_2 [25]. The phase purity of the crystals was confirmed using a Renishaw inVia Raman microscope with backscattering geometry, using a 532-nm wavelength laser with a power of 0.2 W focused through an inverted microscope (Leica) via a $50\times$ objective lens at multiple points across each crystal.

The direct band gaps of the single crystals were determined using PR measurements. During PR measurements, each sample was mounted on a cold finger in a helium closed-cycle refrigerator coupled with a programmable temperature controller, allowing measurements in the 20–320 K temperature range. The reflected light from the sample was dispersed by a single grating 0.55-m focal-length monochromator and detected using a Si photodiode or a thermoelectrically cooled InGaAs p-i-n photodiode. To illuminate the sample, a semiconductor laser (405-nm line) and a 150-W tungsten-halogen bulb were used as the pump and probe beams, respectively. The pump beam was modulated by a mechanical chopper at a frequency of 290 Hz. Phase-sensitive detection of the PR signal was made using a lock-in amplifier.

HAXPES measurements were conducted on as-entered samples at the I09 beamline at Diamond Light Source (DLS), Oxfordshire, UK. The photon energy used for the measurements was 5921 eV, selected by a double-crystal Si (111) monochromator followed by a Si (004) channel-cut high-resolution monochromator. The experimental resolution was determined to be 0.3 eV by fitting a Gaussian-broadened Fermi-Dirac function to the measured Fermi edge of a polycrystalline gold sample. Photoelectrons were measured with a VG Scienta EW4000 electron analyzer with a $\pm 28°$ acceptance angle. All binding energies were referenced to the Fermi level at 0 eV.

The bulk electronic structure of the three Sn sulfide phases was simulated using Kohn-Sham density functional theory (DFT) [26,27] as implemented in the VIENNA AB INITIO SIMULATION PACKAGE [28]. The electron exchange and correlation were modeled using the Perdew-Burke-Enzerhof (PBE) generalized gradient approximation (GGA) functional [29]. Van der Waals forces were accounted for using the DFT-D3 dispersion correction [30] with Becke-Johnson damping [31]. A plane-wave basis with a 550 eV kinetic energy cutoff was used with projector augmented-wave pseudopotentials [32,33] treating the Sn 5s, 4d, and 5p and the S 3s and 3p states as valence electrons. Γ-centred Monkhorst-Pack k-point grids [34] with $8 \times 4 \times 8$, $4 \times 8 \times 3$ and $8 \times 8 \times 6$ subdivisions for SnS, Sn_2S_3, and SnS_2, respectively, were used to sample the Brillouin zones. A convergence criteria of 1×10^{-7} eV on the total energy was used during the electronic minimizations. The cell shape, ion positions, and volume were optimized until the forces on each atom were below 5×10^{-3} eV Å^{-1}. For the calculation of the electronic structure, the HSE06 hybrid functional was used [35–37]. Denser Brillouin zone sampling meshes with $12 \times 6 \times 12$, $6 \times 12 \times 5$, and $12 \times 12 \times 8$ subdivisions (196, 84, and 131 irreducible k points were used for SnS, Sn_2S_3, and SnS_2, respectively, and the integration was performed using the Blöchl-corrected tetrahedron method
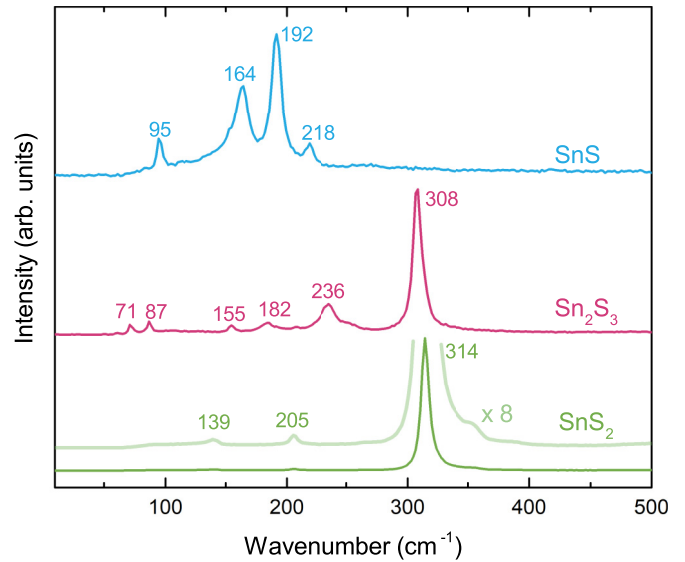

FIG. 3. Raman spectra for all three Sn sulphide phases showing the phase purity of the materials.

[38]. The tolerance on the electronic minimization for these calculations was reduced to 10^{-6} eV.

To calculate the valence band density of states (DOS) of litharge SnO (space group $P4/nmm$), the PBE-GGA functional was used. The total energy of SnO was converged to within 1 meV per atom using a plane-wave energy cutoff of 520 eV and a convergence criteria of 1×10^{-8} eV on the total energy. The Sn 5s, 4d, and 5p and the O 2s and 2p states were treated as valence electrons. A Γ-centered k-point mesh with $21 \times 21 \times 21$ subdivisions was used to sample the Brillouin zone. Geometry optimizations were performed to reduce the forces on each atom to less than 10^{-3} eV Å^{-1}. The PBE-GGA lattice parameters for SnO were $a = 3.8703$ Å and $c = 5.0368$ Å.

To compare the DFT calculation to photoemisson data, the calculated DOS has been cross section corrected [20]. The calculated DOS was also broadened to account for lifetime broadening and instrumental broadening. The Gaussian broadening was kept fixed at 0.3 eV full width at half maximum (FWHM) to represent the instrumental broadening and Lorentzian lifetime broadening was applied to achieve a reasonable fit. The Lorentzian broadening was 0.4 eV for SnS, 0.3 eV for Sn_2S_3, 0.2 eV for SnS_2, and 0.4 eV for SnO.

III. RESULTS AND DISCUSSION

A. Raman spectroscopy—phase determination

Raman spectroscopy was utilized to determine the phases of the crystals, in particular for SnS_2, as it can be found in multiple polytypes: 2H, 4H, and 18R which have similar, but distinct Raman modes between 198 and 220 cm^{-1}. For the 2H SnS_2 polytype, there is only one peak within this range, which is the E_g mode [19].

The Raman spectra for all three phases are shown in Fig. 3. For SnS, the spectrum contains four peaks located at 95 cm^{-1}, 164 cm^{-1}, 192 cm^{-1}, and 218 cm^{-1} in agreement with previous literature [39], indicating orthorhombic SnS (space group
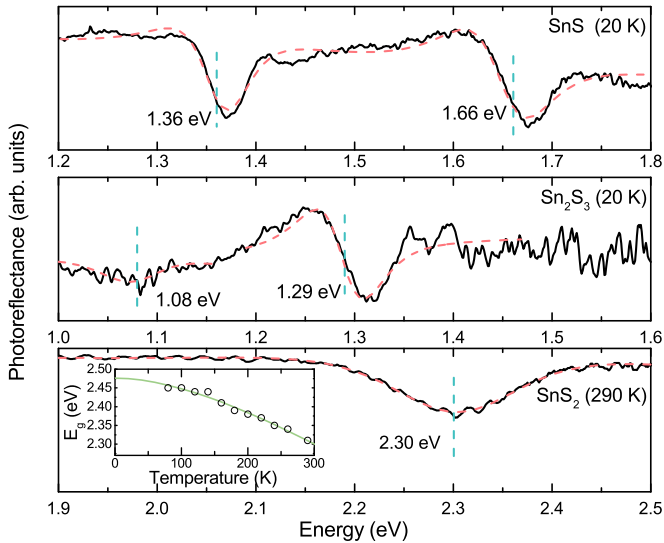
FIG. 4. Photoreflectance data for SnS (top), Sn_2S_3 (middle), and SnS_2 (bottom). The pink dashed line represents the Aspnes fit applied to the data depicted by the black solid line. The transition energies determined from the fits are shown by the vertical dashed blue lines. The inset (bottom left) shows a Varshni fit (solid green line) to the temperature-dependent direct band gap values of SnS_2 from PR to extract the direct band gap at 20 K.

Pnma). The Sn_2S_3 Raman spectrum contains six peaks at 71 cm^{-1}, 87 cm^{-1}, 155 cm^{-1}, 182 cm^{-1}, 236 cm^{-1}, and 308 cm^{-1}, consistent with the orthorhombic crystal structure of Sn_2S_3 (space group *Pnma*) [40]. Finally, the Raman spectrum of SnS_2 has an intense mode at 314 cm^{-1}, and two low-intensity modes at 139 cm^{-1} and 205 cm^{-1}, confirming the 2H hexagonal crystal structure (space group $P\bar{3}m1$) [19], as the 4H and 18R polytypes have multiple modes between 198 and 220 cm^{-1} [41]. The peak positions for all three phases are consistent with DFT-calculated Raman spectra [42]. The vibrational modes observed did not indicate any secondary phases, illustrating the high quality and phase purity of the crystals used for this study.

B. Photoreflectance—band gaps and direct transitions

Photoreflectance was employed to determine the direct band gaps of the crystals. Furthermore, the band gap could be used to corroborate the polytype of the SnS_2 crystal because the 4H polytype has a lower band gap than 2H [43–45].

The PR data is shown in Fig. 4 where an Aspnes fit [46] is applied to extract the band gap for direct interband transitions. However, for SnS_2, a PR signal could not be obtained at 20 K. Therefore, a Varshni fit [47] was used to model the temperature dependence of the band gap from PR data recorded between 290 and 80 K to extrapolate to a band gap at 20 K. This was found to be 2.47 eV with the Varshni equation parameters $\alpha = 1.27 \times 10^{-3}$ eV K^{-1}, $\beta = 350.09$ K, and $E_{g0} = 2.476$ eV.

SnS can be seen to have two very strong features in its PR spectrum, corresponding to direct transitions at 1.36 and 1.66 eV, which are consistent with the E_0 and E_1 direct transitions previously reported from ellipsometry and elec-

troreflectance measurements [48,49]. These transitions corresponded to direct transitions between the valence band and conduction band along the Γ to Y direction and the Γ to X direction, respectively, which can be seen in Fig. 3 of Ref. [48].

As no PR data for Sn_2S_3 has been reported previously in the literature, it is used here to determine the lowest energy direct transitions of Sn_2S_3. Sn_2S_3 shows two PR features, the main feature being at 1.29 eV with a weaker feature at 1.08 eV. The literature reports many values for the band gap and lowest energy optical transitions for Sn_2S_3, ranging from 0.95 to 2 eV. This range is due to different approaches to the data analysis, whereby different types of optical transition were assumed, and also to sample variation between studies [50–53]. The lower literature band gap values (0.95, 1.08, and 1.16 eV) are reported as direct forbidden transitions which would be expected to be weak. Indeed, the PR spectrum for Sn_2S_3 has lower signal-to-noise ratio compared to the other two phases, as a consequence of the weaker signals associated with two forbidden direct transitions. The finding of two direct transitions is consistent with the the work of Sanchez-Juarez and Ortíz [51], where two absorption onsets were observed with the lower energy one being much weaker than the other. Singh also reported a weak direct transition at 0.97 eV from the calculated band structure similar to what is seen in experiments [54].

SnS_2 was found to have a room-temperature direct band gap of 2.30 eV and an 80 K value of 2.45 eV which are consistent with the 2H polytype and not the 4H, as the 4H polytype has been reported to have slightly lower band gap values of 2.15 eV and 2.30 eV at room temperature and at 77 K, respectively [43]. The direct band gap at 20 K was estimated from the Varshni fit to be 2.47 eV, consistent with Powell's findings for 2H SnS_2 [43]. The fundamental direct band gap has been found from DFT to be at the M point and within the range of 2.16–2.77 eV. This spread of reported values is largely due to the different treatments applied to account for the van der Waals interactions [19,55,56].

Thus, the three fundamental direct band gaps for SnS, Sn_2S_3, and SnS_2 were found to be 1.36, 1.08, and 2.47 eV at 20 K. While these values from PR are consistent with previous literature [43,51,57,58], they represent clearer direct band-gap determinations than for much of the prior work. Interpretation of PR data is somewhat less ambiguous than for both optical absorption derived from transmission and reflection data and spectroscopic ellipsometry with the complexiy of the modeling involved. This is particularly the case for Sn_2S_3, for which reports of optical properties are scarce. As PR does not give information on the indirect transitions, the 0 K indirect band gaps determined from the calculations presented here are SnS, 1.11 eV, Sn_2S_3, 1.09 eV, and SnS_2, 2.24 eV [24].

C. HAXPES and theoretical DOS

The core level spectra for all three tin sulphide phases were obtained using HAXPES. The binding energies and FWHM values of the core level peaks are presented in Table I. The most intense core level lines for Sn and S, Sn $3d_{5/2}$, and S $2p$ are shown in Figs. 5 and 6.

TABLE I. Core-level binding energies with full width at half maximum (FWHM) in brackets for Sn $3d_{5/2}$ peaks corresponding to Sn(II) and Sn(IV) and S $2p_{3/2}$ peaks in SnS, Sn_2S_3, and SnS_2.

	Sn (II) $3d_{5/2}$ (FWHM) (eV)	Sn (IV) $3d_{5/2}$ (FWHM) (eV)	S $2p_{3/2}$ (FWHM) (eV)
SnS	485.6 (0.62)		161.2 (0.64)
Sn_2S_3	485.8 (0.70)	486.3 (0.62)	161.4 (0.68)
SnS_2		486.6 (0.67)	161.7 (0.72)

The Sn $3d_{5/2}$ spectra identify the different oxidation states of Sn where the binding energies of the two states are seen to vary significantly. Figure 5 shows the Sn $3d_{5/2}$ for all three sulphides where panel (a) is that of SnS, panel (b) is for Sn_2S_3, and panel (c) is that of SnS_2. The fit of the full $3d$ region including the $3d_{3/2}$ can be seen in Fig. S1 of the Supplemental Material (SM) [59].

For SnS, in Fig. 5(a), where the Sn is in the +2 oxidation state, the binding energy of the main peak is 485.6 eV with an additional peak due to oxide contamination at 486.4 eV [60]. The secondary peak is attributed to SnO [60,61], corresponding to Sn remaining in the same 2+ oxidation state and consistent with the presence of an O $1s$ peak in the survey spectrum (not shown). The Sn-O component is at higher binding energy than the Sn-S component due to the higher electronegativity of oxygen compared with sulfur.

For SnS_2, in Fig. 5(c), where the Sn is in the +4 oxidation state, the main core-level peak is at 486.6 eV. A very weak, secondary peak was also required at 485.7 eV which is thought to be some Sn(II) contamination at the surface. The Raman spectrum did not show any modes that would suggest that SnS was present, therefore we attribute this to a very small amount of Sn(II) only at the surface.

Comparing the binding energies of the Sn $3d_{5/2}$ components in Figs. 5(a) and 5(b), we see a significant difference in the peaks associated with the two oxidation states of Sn. Thus, two Sn $3d$ components are expected from the two different Sn oxidation states in Sn_2S_3. While Sn(II) and Sn(IV) com-

FIG. 6. HAXPES spectra of the S $2p$ region along with the Voigt function fitting of the components for all three Sn-sulphide phases.

ponents were readily identified in early x-ray photoemission spectroscopy (XPS) of tin oxides [62], a more recent report on Sn(II) and Sn(IV) iodide perovskites suggested they are not easily distinguished due to the degree of overlap of their XPS Sn $3d$ component [63]. From these previous studies, it seems likely that two different Sn $3d$ components corresponding to the two different Sn oxidation states will be straightforwardly discernible by curve fitting the Sn $3d$ spectra.

Indeed, in Fig. 5(b), two contributions to the Sn $3d_{5/2}$ core-level spectrum of Sn_2S_3 are found at binding energies of 485.8 eV and 486.3 eV for Sn(II) and Sn(IV), respectively. This 0.5 eV difference in binding energy of the core levels compared to the 1.0 eV difference between Sn(II) in SnS and Sn(IV) in SnS_2 is explained by the fact that the Sn(II) will experience stronger bonding due to the presence of Sn(IV) [23]. The area ratio of the two peaks is 1:1, as expected for the Sn_2S_3 structure. While this provides still further evidence of the experimental existence of the Sn_2S_3 phase, the phase is found to be unstable in DFT for many functionals [42,64]. The formation energy of Sn_2S_3 is generally found to be above the tin sulphide convex hull, the bounding surface between the lowest energy phases of each composition. For DFT to find Sn_2S_3 to be stable requires an appropriate treatment of both dispersion interactions and vibrational contributions to the free energy [42]. With such considerations becoming more routine in DFT studies, Sn_2S_3 may now achieve greater attention than previously, from both theoretical and experimental perspectives.

While the two Sn environments within Sn_2S_3 can be resolved, it can be seen in Fig. 5(b) that the Sn $3d_{5/2}$ line shape is asymmetric at both higher and lower binding energies, suggesting that there are other contributions to the spectrum. Therefore, a very low intensity component at lower binding energy was added to the fit and is thought to be due to unreacted Sn, for which the binding energy is 484.8 eV, in agreement with previous studies [61]. At high binding energy, initially one component was added that was found to be 1 eV higher than the Sn(II) component and 0.5 eV higher than the Sn(IV) component. These values were too high and too
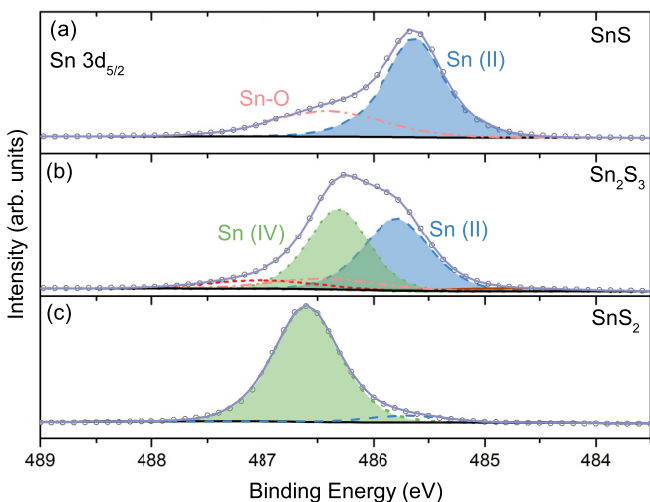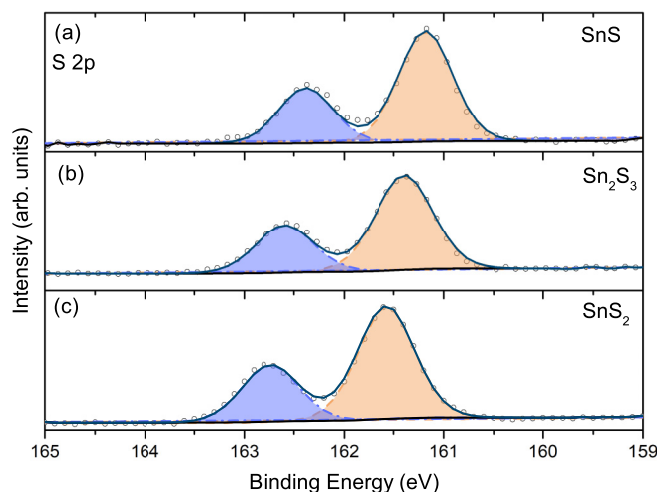

FIG. 5. HAXPES spectra of the Sn $3d_{5/2}$ along with the Voigt function fitting of the components for all three Sn sulphide phases.
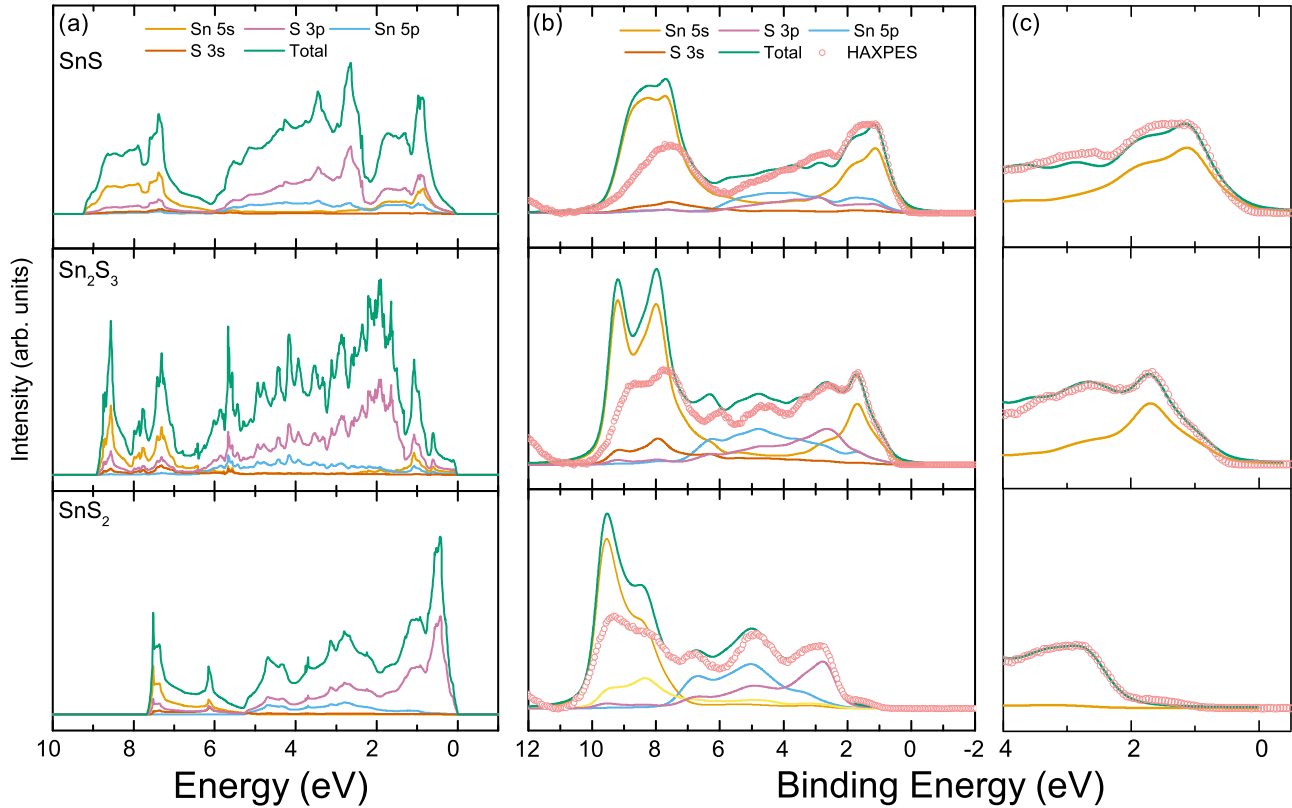
FIG. 7. (a) Calculated density of states for all three Sn sulphides, where the VBM is set at zero, (b) measured HAXPES valence band spectra from the different tin sulphide phases compared with the cross-section corrected and broadened calculated density of states, and (c) top of the valence band zoomed in to emphasize the region where the Sn 5*s* lone pair states contribute.

low, respectively, to be the oxide of Sn(II) and Sn(IV), which suggested that this was an average of two oxides, one for each of the Sn oxidation states. Therefore, two oxide peaks were included in the fit, 0.5 eV apart (the same as the two different Sn-sulphide components), one for Sn(II)-oxide and one for the Sn(IV)-oxide environment. The two fitted oxide peaks were both found to be at 0.7 eV higher binding energy than the corresponding Sn-sulphide component. The separation between the sulphide and oxide component binding energies is in agreement with literature [23]. The extent of the oxide contamination of the three different Sn sulphides appears to be correlated with the proportion of Sn(II) in each of the phases, where in SnS the percentage of Sn-O signal is 31%, 9% in Sn_2S_3, and 0% in SnS_2. This indicates that the presence of lone pairs results in the surface of the material being more reactive and therefore more readily contaminated.

The S 2*p* core-level spectra for the three tin sulphide crystals are shown in Fig. 6. For all three phases, only one sulfur component is present in the S 2*p* region with a doublet separation of 1.2 eV and an area ratio of 2:1 between the $2p_{3/2}$ and $2p_{1/2}$ components. It can be seen that the binding energy increases from SnS to Sn_2S_3 to SnS_2 which follows the trend of increasing VBM to the Fermi-level shift (discussed below). There is also the chemical shift that could affect this due to the different Sn-S bonding environments in the different tin sulphides. Therefore, the shift is most likely to be a combination of these factors. This component corresponds in each case to the S^{2-} in tin sulphide; no peaks due to contaminants are present.

From analysis of the core-level photoemission of these materials, the phases of the Sn sulphides can be successfully identified. However, the most information-rich part of photoemission data lies in the valence band spectra. From the core-level analysis and Raman analysis, the phases of the samples have been confirmed and, therefore, the valence band spectra can be compared with the calculated DOS.

Figure 7 shows the unbroadened calculated DOS in panel (a), the measured HAXPES and calculated valence band spectra in panel (b), and a magnification in panel (c). The experimental data is plotted with respect to the Fermi level at 0 eV and the cross-section corrected and broadened calculated DOS is shifted to align to the data. In general, all three phases show very good agreement between theory and experiment with all spectral features being present in both and the relative intensities match reasonably well. The discrepancies come at higher binding energy, which is expected due to stronger final-state relaxation effects for more strongly bound orbitals [65]. Therefore, the broadening applied at the top of the valence band is insufficient for deeper states, such as those around 8 eV.

It was seen that there was a small contribution from the semicore Sn 4*d* states to the valence band DOS of all three of the phases. However, comparing the numerical integrals of the total and orbital-projected Sn and S DOS, which give the electron counts, shows that this contribution is most likely an artifact (full details can be found on page 3 of the SM). Therefore, these orbitals were not included when comparing the theoretical DOS to the experimental DOS. Further to

this, the measured Sn $4d$ semicore levels were plotted and compared to the calculated (Fig. S8) ones. This showed that the experimental core levels are found to be at higher binding energy than in the calculation. This means that the intensity of the d levels in the experimental valence band spectrum is expected to be even smaller than in the calculation, further strengthening the argument to remove the calculated d states for comparison to the experimental valence band DOS. To compare the measured DOS to the calculation, the experimental background was subtracted, as the calculated DOS does not take into account the inelastic scattering of photoelectrons that contributes to the background in XPS. However, for comparison with Ref. [23], the raw data is plotted in Fig. S9 in the SM.

To provide more detail, each phase will now be discussed individually. First, it is apparent from Fig. 7(b) (top) that the theoretical DOS for SnS is in good agreement with the experimental valence band spectrum. The features present in the HAXPES measurement are present in the DFT calculation at very similar energies. From the core-level analysis in Fig. 5(a), it is apparent that up to 31% of the measured spectral signal originates from SnO. Hence, SM Fig. S10 shows the combination of 31% SnO valence band DOS and 69% of SnS valence band DOS. The difference is small between the combined SnO and SnS DOS and the SnS DOS. Therefore, for simplicity only. the SnS DOS is used in Fig. 7.

Examining the different regions of the spectra in turn to see the different orbital contributions, between 10 and 6 eV consists mainly of Sn $5s$ and Sn $5p$ features. There is a large Sn $5s$ contribution, but also a contribution from S $3p$, indicating that the two orbitals are hybridized, as expected. There is also a small hybridization component from the Sn $5p$ and S $3s$. Moving to the middle of the valence band, between 6 and 2 eV, it is seen that the main contribution is from S $3p$, Sn $5p$, and Sn $5s$. Further down toward the valence band edge, a strong Sn $5s$ feature dominates with hybridization with S $3p$ and Sn $5p$ states. This s-state feature has much greater relative strength than when soft x rays are used [23] due to the slower fall off of the photoionization cross section of s states with photon energy than other orbitals. Thus, the s states are very prominent in these HAXPES measurements.

The center panel of Fig. 7(b) displays the theoretical and experimental valence band DOS of Sn_2S_3. Sn_2S_3 exhibits similar hybridization between the Sn $5s$ and S $3p$ to SnS and exhibits the signature $5s$ lone pair at the valence band edge. However, the intensity of the lone-pair feature is not as strong as that in SnS. This is because only half of the Sn atoms possess a filled lone pair, i.e., those in the Sn(II) oxidation state and not the Sn(IV) atoms.

The calculated and experimental valence band DOS of SnS_2 are seen in the bottom panel of Fig. 7(b). Because the electron density is symmetric around the Sn atoms, there is no indication of sp hybridization in this case due to it being symmetry forbidden. Therefore, the Sn $5s$ orbitals are unoccupied and thus do not contribute at the valence band edge (0–2 eV) but instead contribute between 10 and 6 eV, similar to in SnS, and in the conduction band. The main contribution to the valence band is the sulfur $3p$ orbitals, which contribute across the whole valence band. In the middle of the valence band, there are also Sn $5p$ and S $3p$ contributions. As mentioned

previously, some low-level Sn(II) contamination was found when fitting the Sn $3d_{5/2}$ core levels; evidence of this is seen in the valence band where there is a small intensity above the VBM at a binding energy of ∼1 eV.

In the context of the revised lone pair model [9], for SnS and Sn_2S_3 the Sn $5s$ orbitals are able to interact with the S p orbitals. This explains the structures seen in Fig. 1 as they both possess a void within the structure into which the lone pairs project. As discussed in the Introduction, the interaction between these orbitals is usually forbidden due to the crystal symmetry, but the distortion of the crystal means that the interaction is symmetry allowed.

From this study, it can be seen how effective hard XPS is for obtaining experimental evidence of ns^2 lone pair contributions to the valence band DOS. When comparing figures for soft and hard XPS ([23] and Fig. 7(b), respectively), the s-state contribution dominates the HAXPES valence band spectrum, especially at the valence band edge, when lone-pair s states are present.

The lack of a lone pair in SnS_2 can be seen, particularly clearly in Fig. 7(c), to drastically change the position of the VBM with respect to the other two phases. The energy separations from the VBMs to the Fermi levels were obtained by extrapolating the valence band edge (see Fig. S11 of the SM); these values were found to be 0.35, 0.69, and 1.97 eV for SnS, Sn_2S_3, and SnS_2, respectively. The effect of this can be seen to increase the band gap, as is evident from the PR measurements where the band gap of SnS_2, with no lone pairs, is more than 1 eV greater than that of SnS and Sn_2S_3. A further implication of this is that the band alignment of the tin sulphides is very phase-dependent. The band alignments have been previously measured by Whittles *et al.* [23], where SnS and Sn_2S_3 were shown to have a significantly higher VBM with respect to the vacuum level than SnS_2.

IV. CONCLUSION

A PR, HAXPES, and DFT study of the electronic structure of the different Sn sulphide phases has been presented. The PR measurements reveal the fundamental direct band gaps of three phases to be 1.36, 1.08, and 2.47 eV for SnS, Sn_2S_3, and SnS_2 respectively. To investigate the Sn $5s$ lone-pair states that feature prominently at the top of the SnS and Sn_2S_3 valence band, HAXPES valence band measurements and density functional theory were combined. This allowed a clearer elucidation of the Sn $5s$ lone-pair contribution to the electronic structure of these materials than previously obtained using only soft x-ray photoemission. The DFT DOS show good agreement with the experimental data and confirm the varying nature of the Sn $5s$ state, depending on the electron configurations/oxidation states of the Sn atoms in the different Sn-sulphide phases. These results, along with those in Ref. [23], highlight how effective using a combination of photon energies is for probing ns^2 lone pairs due to the varying intensity of the relative photoionization cross sections of s orbitals with respect to those of p and d orbitals.

Additionally, the core-level photoemission data presented highlight the potential of photoemission techniques, both XPS and HAXPES, to distinguish the presence or absence of, and relative proportions of, Sn(II) and Sn(IV) species. This is

not only relevant to studies of the Sn sulphides, but also to work on other Sn-containing materials including inorganic and hybrid perovskites and CZTS.

ACKNOWLEDGMENTS

[1] Z. Ran, X. Wang, Y. Li, D. Yang, X.-G. Zhao, K. Biswas, D. J. Singh, and L. Zhang, Bismuth and antimony-based oxyhalides and chalcohalides as potential optoelectronic materials, npj Comp. Mater. **4**, 14 (2018).

[2] K. Sayama, A. Nomura, Z. Zou, R. Abe, Y. Abe, and H. Arakawa, Photoelectrochemical decomposition of water on nanocrystalline $BiVO_4$ film electrodes under visible light, Chem. Commun. **23**, 2908 (2003).

[3] I. C. Vinke, J. Diepgrond, B. A. Boukamp, K. J. de Vries, and A. J. Burggraaf, Bulk and electrochemical properties of $BiVO_4$, Solid State Ionics **57**, 83 (1992).

[4] D. J. Payne, R. G. Egdell, G. Paolicelli, F. Offi, G. Panaccione, P. Lacovig, G. Monaco, G. Vanko, A. Walsh, G. W. Watson, J. Guo, G. Beamson, P.-A. Glans, T. Learmonth, and K. E. Smith, Nature of electronic states at the fermi level of metallic $\beta-PbO_2$ revealed by hard x-ray photoemission spectroscopy, Phys. Rev. B **75**, 153102 (2007).

[5] A. M. Ganose, C. N. Savory, and D. O. Scanlon, Beyond methylammonium lead iodide: Prospects for the emergent field of ns^2 containing solar absorbers, Chem. Commun. **53**, 20 (2017).

[6] E. Peccerillo and K. Durose, Copper-antimony and copper-bismuth chalcogenides-research opportunities and review for solar photovoltaics, MRS Energy & Sustainability **5**, E13 (2018).

[7] T. J. Whittles, T. D. Veal, C. N. Savory, A. W. Welch, F. W. de Souza Lucas, J. T. Gibbon, M. Birkett, R. J. Potter, D. O. Scanlon, A. Zakutayev, and V. R. Dhanak, Core levels, band alignments, and valence-band states in $CuSbS_2$ for solar cell applications, ACS Appl. Mater. Interfaces **9**, 41916 (2017).

[8] T. J. Whittles, T. D. Veal, C. N. Savory, P. J. Yates, P. A. E. Murgatroyd, J. T. Gibbon, M. Birkett, R. J. Potter, J. D. Major, K. Durose, D. O. Scanlon, and V. R. Dhanak, Band alignments, band gap, core levels, and valence band states in Cu_3BiS_3 for photovoltaics, ACS Appl. Mater. Interfaces **11**, 27033 (2019).

[9] A. Walsh, D. J. Payne, R. G. Egdell, and G. W. Watson, Stereochemistry of post-transition metal oxides: Revision of the classical lone pair model, Chem. Soc. Rev. **40**, 4455 (2011).

[10] M. Devika, N. K. Reddy, K. Ramesh, R. Ganesan, K. R. Gunasekhar, E. S. Gopal, and K. T. Reddy, Thickness effect on the physical properties of evaporated SnS films, J. Electrochem. Soc. **154**, H67 (2007).

[11] A. Tanuŝevski and D. Poelman, Optical and photoconductive properties of SnS thin films prepared by electron beam evaporation, Sol. Energy Mater. Sol. Cells **80**, 297 (2003).

[12] M. Sugiyama, T. Shimizu, D. Kawade, K. Ramya, and K. T. Ramakrishna Reddy, Experimental determination of vacuum-level band alignments of SnS-based solar cells by photoelectron yield spectroscopy, J. Appl. Phys. **115**, 083508 (2014).

[13] K. R. Reddy, N. K. Reddy, and R. Miles, Photovoltaic properties of SnS based solar cells, Sol. Energy Mater. Sol. Cells **90**, 3041 (2006).

[14] H. Yun, B. Park, Y. C. Choi, J. Im, T. J. Shin, and S. I. Seok, Efficient nanostructured TiO_2/SnS heterojunction solar cells, Adv. Energy Mater. **9**, 1901343 (2019).

[15] S. Kim, J.-S. Ji-Sang Park, S. N. Hood, and A. Walsh, Lone-pair effect on carrier capture in Cu_2ZnSnS_4 solar cells, J. Mater. Chem. A **7**, 2686 (2019).

[16] Y. Sun, H. Cheng, S. Gao, Z. Sun, Q. Liu, Q. Liu, F. Lei, T. Yao, J. He, S. Wei, and Y. Xie, Freestanding tin disulfide single-layers realizing efficient visible-light water splitting, Angew. Chem. Int. Ed. **51**, 8727 (2012).

[17] X. Hu, G. Song, W. Li, Y. Peng, L. Jiang, Y. Xue, Q. Liu, Z. Chen, and J. Hu, Phase-controlled synthesis and photocatalytic properties of SnS, SnS_2, and SnS/SnS_2 heterostructure nanocrystals, Mater. Res. Bull. **48**, 2325 (2013).

[18] N. Deshpande, A. Sagade, Y. Gudage, C. Lokhande, and R. Sharma, Growth and characterization of tin disulfide (SnS_2) thin film deposited by successive ionic layer adsorption and reaction (SILAR) technique, J. Alloys and Compounds **436**, 421 (2007).

[19] L. A. Burton, T. J. Whittles, D. Hesp, W. M. Linhart, J. M. Skelton, B. Hou, R. F. Webster, G. O'Dowd, C. Reece, D. Cherns, D. J. Fermin, T. D. Veal, V. R. Dhanak, and A. Walsh, Electronic and optical properties of single crystal SnS_2: An earth-abundant disulfide photocatalyst, J. Mater. Chem. A **4**, 1312 (2016).

[20] J. H. Scofield, Theoretical Photoionization Cross Sections from 1 to 1500 keV, Tech. Rep. (Lawrence Livermore Laboratory, United States, Jan 1973) uCRL–51326, pp. 48–49 and 129–131.

[21] J. J. Yeh and I. Lindau, Atomic subshell photoionization cross sections and asymmetry parameters: $1 \leqslant z \leqslant 103$, At. Data Nucl. Data Tables **32**, 1 (1985).

[22] P. Day, A. Hamnett, and A. F. Orchard, Photoelectron spectroscopy, in *Electronic Structure and Magnetism of Inorganic*

Compounds, Vol. 3, edited by P. Day (The Chemical Society, London, 1974), Chap. 4, pp. 218–415.

[23] T. J. Whittles, L. A. Burton, J. M. Skelton, A. Walsh, T. D. Veal, and V. R. Dhanak, Band alignments, valence bands, and core levels in the tin sulfides SnS, SnS_2, and Sn_2S_3: Experiment and theory, Chem. Mater. **28**, 3718 (2016).

[24] L. A. Burton, D. Colombara, R. D. Abellon, F. C. Grozema, L. M. Peter, T. J. Savenije, G. Dennler, and A. Walsh, Synthesis, characterization, and electronic structure of single-crystal SnS, Sn_2S_3, and SnS_2, Chem. Mater. **25**, 4908 (2013).

[25] T. Shibata, T. Miura, T. Kishi, and T. Nagai, Synthesis of single crystal SnS_2 by chemical vapor transport method at low temperature using reverse temperature gradient, J. Cryst. Growth **106**, 593 (1990).

[26] P. Hohenberg and W. Kohn, Inhomogeneous electron gas, Phys. Rev. **136**, B864 (1964).

[27] W. Kohn and L. J. Sham, Self-consistent equations including exchange and correlation effects, Phys. Rev. **140**, A1133 (1965).

[28] G. Kresse and J. Hafner, Ab initio molecular dynamics for liquid metals, Phys. Rev. B **47**, 558 (1993).

[29] J. P. Perdew, K. Burke, and M. Ernzerhof, Generalized Gradient Approximation Made Simple, Phys. Rev. Lett. **77**, 3865 (1996).

[30] S. Grimme, J. Antony, S. Ehrlich, and H. Krieg, A consistent and accurate ab initio parametrization of density functional dispersion correction (DFT-D) for the 94 elements H-Pu, J. Chem. Phys. **132**, 154104 (2010).

[31] S. Grimme, S. Ehrlich, and L. Goerigk, Effect of the damping function in dispersion corrected density functional theory, J. Comp. Chem. **32**, 1456 (2011).

[32] P. E. Blöchl, Projector augmented-wave method, Phys. Rev. B **50**, 17953 (1994).

[33] G. Kresse and D. Joubert, From ultrasoft pseudopotentials to the projector augmented-wave method, Phys. Rev. B **59**, 1758 (1999).

[34] H. J. Monkhorst and J. D. Pack, Special points for brillouin-zone integrations, Phys. Rev. B **13**, 5188 (1976).

[35] A. V. Krukau, O. A. Vydrov, A. F. Izmaylov, and G. E. Scuseria, Influence of the exchange screening parameter on the performance of screened hybrid functionals, J. Chem. Phys. **125**, 224106 (2006).

[36] J. Heyd, G. E. Scuseria, and M. Ernzerhof, Hybrid functionals based on a screened Coulomb potential, J. Chem. Phys. **118**, 8207 (2003).

[37] J. Heyd, G. E. Scuseria, and M. Ernzerhof, Hybrid functionals based on a screened Coulomb potential, J. Chem. Phys. **124**, 219906 (2006).

[38] P. E. Blöchl, O. Jepsen, and O. K. Andersen, Improved tetrahedron method for Brillouin-zone integrations, Phys. Rev. B **49**, 16223 (1994).

[39] M. Li, Y. Wu, T. Li, Y. Chen, H. Ding, Y. Lin, N. Pan, and X. Wang, Revealing anisotropy and thickness dependence of Raman spectra for SnS flakes, RSC Adv. **7**, 48759 (2017).

[40] H. R. Chandrasekhar and D. G. Mead, Long-wavelength phonons in mixed-valence semiconductor $Sn^{II}Sn^{IV}S_3$, Phys. Rev. B **19**, 932 (1979).

[41] S. Nakashima, H. Katahama, and A. Mitsuishi, The effect of polytypism on the vibrational properties of SnS_2, Physica B+C **105**, 343 (1981).

[42] J. M. Skelton, L. A. Burton, A. J. Jackson, F. Oba, S. C. Parker, and A. Walsh, Lattice dynamics of the tin sulphides SnS_2, SnS, and Sn_2S_3: Vibrational spectra and thermal transport, Phys. Chem. Chem. Phys. **19**, 12452 (2017).

[43] M. J. Powell, The effect of pressure on the optical properties of 2H and 4H SnS_2, J. Phys. C: Solid State Phys. **10**, 2967 (1977).

[44] S. Acharya and O. N. Srivastava, Electronic bandgap measurements of SnS_2 polytypes, Phys. Stat. Sol. (a) **56**, K1 (1979).

[45] M. J. Powell, E. A. Marseglia, and W. Y. Liang, The effect of polytypism on the band structure of SnS_2, J. Phys. C: Solid State Phys. **11**, 895 (1978).

[46] D. Aspnes, Third-derivative modulation spectroscopy with low-field electroreflectance, Surface Science **37**, 418 (1973).

[47] Y. P. Varshni, Temperature dependence of the energy gap in semiconductors, Physica **34**, 149 (1967).

[48] R. E. Banai, L. A. Burton, S. G. Choi, F. Hofherr, T. Sorgenfrei, A. Walsh, B. To, A. Cröll, and J. R. S. Brownson, Ellipsometric characterization and density-functional theory analysis of anisotropic optical properties of single-crystal α-SnS, J. Appl. Phys. **116**, 013511 (2014).

[49] G. Valiukonis, D. A. Guseinova, G. Keivaitb, and A. Sileika, Optical spectra and energy band structure of layer-type $A^{IV}B^{VI}$ compounds, Phys. Status Solidi (b) **135**, 299 (1986).

[50] S. López, S. Granados, and A. Ortíz, Spray pyrolysis deposition of thin films, Semicond. Sci. Technol. **11**, 433 (1996).

[51] A. Sanchez-Juarez and A. Ortíz, Effects of precursor concentration on the optical and electrical properties of $Sn_X S_Y$ thin films prepared by plasma-enhanced chemical vapour deposition, Semicond. Sci. Technol. **17**, 931 (2002).

[52] U. Alpen, J. Fenner, and E. Gmelin, Semiconductors of the type $Me^{II}Me^{IV}S_3$, Mater. Res. Bull. **10**, 175 (1975).

[53] R. D. Engelken, H. E. McCloud, C. Lee, M. Slayton, and H. Ghoreishi, Low temperature chemical precipitation and vapor deposition of Sn_xS thin films, J. Electrochem. Soc. **134**, 2696 (1987).

[54] D. J. Singh, Optical and electronic properties of semiconducting Sn_2S_3, Appl. Phys. Lett. **109**, 032102 (2016).

[55] J. M. Gonzalez and I. I. Oleynik, Layer-dependent properties of SnS_2 and $SnSe_2$ two-dimensional materials, Phys. Rev. B **94**, 125443 (2016).

[56] X. Wang, Z. Liu, X.-G. Zhao, J. Lv, K. Biswas, and L. Zhang, Computational design of mixed-valence tin sulfides as solar absorbers, ACS Appl. Mater. Interfaces **11**, 24867 (2019).

[57] T. Raadik, M. Grossberg, J. Raudoja, R. Traksmaa, and J. Krustok, Temperature-dependent photoreflectance of SnS crystals, J. Phys. Chem. Solids **74**, 1683 (2013).

[58] S. J. Zelewski and R. Kudrawiec, Photoacoustic and modulated reflectance studies of indirect and direct band gap in van der Waals crystals, Sci. Rep. **7**, 15365 (2017).

[59] See Supplemental Material at http://link.aps.org/supplemental/10.1103/PhysRevMaterials.4.074602 for a plot of the full Sn $3d$ region, details of the DFT DOS and the Sn d contribution, a comparison of the Sn $4d$ semi-core states from experiment and calculations, and the valence band spectra without background subtraction, the combined SnO and SnS valence band DOS from calculations and the linear extrapolations used to determine the VBM energy with respect to the Fermi level.

[60] M. Fondell, M. Gorgoi, M. Boman, and A. Lindblad, An HAX-PES study of Sn, SnS, SnO, and SnO_2, J. Electron Spectros. Relat. Phenom. **195**, 195 (2014).

[61] L. Kövér, Z. Kovács, R. Sanjinés, G. Moretti, I. Cserny, G. Margaritondo, J. Pálinkás, and H. Adachi, Electronic structure of tin oxides: High-resolution study of XPS and Auger spectra, Surf. Int. Anal. **23**, 461 (1995).

[62] L. Jie and X. Chao, XPS examination of tin oxide on float glass surface, J. Non-Cryst. Solids **119**, 37 (1990).

[63] Y. El Ajjouri, F. Locardi, M. C. Gélvez-Rueda, M. Prato, M. Sessolo, M. Ferretti, F. C. Grozema, F. Palazon, and H. J.

Bolink, Mechanochemical synthesis of Sn(II) and Sn(IV) iodide perovskites and study of their structural, chemical, thermal, optical, and electrical properties, Energy Technol. **8**, 1900788 (2019).

[64] Y. Kumagai, L. A. Burton, A. Walsh, and F. Oba, Electronic structure and defect physics of tin sulfides: SnS, Sn_2S_3, and SnS_2, Phys. Rev. Appl. **6**, 014009 (2016).

[65] L. Ley, R. A. Pollak, F. R. McFeely, S. P. Kowalczyk, and D. A. Shirley, Total valence-band densities of states of III-V and II-VI compounds from x-ray photoemission spectroscopy, Phys. Rev. B **9**, 600 (1974).